Inorganic Chemistry

pubs.acs.org/IC Article

# Electronic Structure Study of Rhombic $Mn^{II}$ Complexes with Hexadentate $N_4O_2$ Chelate Ligands

Conor T. Kelly, Brittany Grimm, Eimear Harrison, Vibe B. Jakobsen, Ross Jordan, Solveig Felton, Helge Müller-Bunz, Stephen Hill,* and Grace G. Morgan*

**Cite This:** *Inorg. Chem.* 2026, 65, 6464−6475 **Read Online**

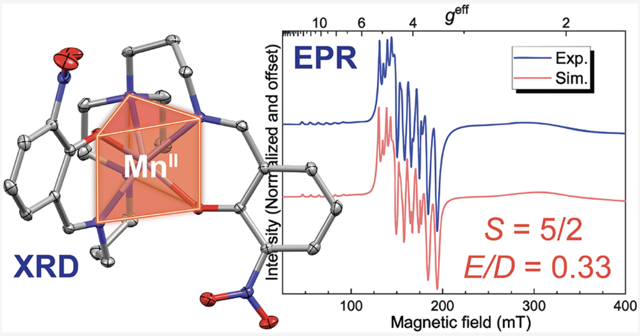

**ABSTRACT:** Herein, we investigate the structural and electronic properties of nine mononuclear $Mn^{II}$ complexes with Schiff base ligands synthesized from *R*-salicylaldehyde and 1,4-bis(3-aminopropyl)piperazine which readily adopt a distorted trigonal prismatic geometry, where the *R* groups are 3-$NO_2$ (**1**), 3-$NO_2$-5-OMe (**2**), 3-$NO_2$-5-Cl (**3**), 3-Br-5-$NO_2$ (**4**), 3-OMe-5-$NO_2$ (**5**), 5-$NO_2$ (**6**), 3,5-diCl (**7**), 3,5-diBr (**8**), and 3,5-diI (**9**). We utilize Continuous Shape Measure to quantify the degree of geometric distortion relative to other structures published in the Cambridge Structural Database (CSD). X-band EPR spectroscopy indicated atypical anisotropy and higher-field and frequency measurements were used to quantify the zero-field splitting (ZFS) parameters. Simulations of the spectra revealed axial and rhombic ZFS parameters, $D = +0.200(2)\ \mathrm{cm}^{-1}$ and $|E| = 0.067(2)\ \mathrm{cm}^{-1}$, for a frozen solution of **1**. Despite the trigonal geometry of the $Mn^{II}$ coordination environment, EPR data indicate a rhombic electronic structure with an $E/D$ ratio at the rhombic limit of 0.33. This is ascribed to the different identity of the coordinating atoms (two nitrogens and one oxygen) associated with the triangular faces of the trigonal prism, i.e., even though the coordination geometry is close to trigonal, the ligand field symmetry is not.

## ■ INTRODUCTION

Electron paramagnetic resonance (EPR) spectroscopy can offer valuable insight into the electronic structure of paramagnetic complexes, where determination of zero-field splitting (ZFS) parameters facilitates understanding of magnetic anisotropy and its relation to structure.[1,2] In general, understanding the ZFS parameters in transition metal complexes yields valuable insights into their electronic structure and can be used to better understand their use as single ion magnets (SIMs),[3−5] as magnetic resonance imaging (MRI) contrast agents,[6,7] as magnetic refrigerants showing the magnetocaloric effect (MCE),[5,8] or in the development of structure−property relationships to explore sites with unknown structures, especially in biochemistry.[1,9] For cases of six-coordinate octahedral (or *pseudo*-octahedral) $Mn^{II}$ an isotropic signal at $g^{eff} = 2$ is typically observed, where the magnitude of the ZFS parameters is small.[10] The ZFS parameters, however, are sensitive to the environment of the $Mn^{II}$ ion and depend on the coordination number, geometry, and nature of the ligands.[1,2,10] Values of $D$ are typically less than 1 $\mathrm{cm}^{-1}$, with the largest reported value of $D = +1.460\ \mathrm{cm}^{-1}$ for a polyoxometalate complex.[11] Aside from this example, complexes with coordinated halides typically show the largest $D$ values for $Mn^{II}$ systems,[10] and those with N/O based ligands have values more in the region of $D < 0.2\ \mathrm{cm}^{-1}$.[2] Duboc notes that the magnitude of $D$ in $Mn^{II}$ systems with N,O-based ligands is sensitive to both the coordination number and the ligand denticity,[2,10] which has relevance in $Mn^{II}$ based metalloenzymes with N,O-based active sites.[9,12−20] A clear understanding of the ZFS parameters has informed the design of $Mn^{II}$ based MRI contrast agents,[21,22] for which there has been renewed interest due to the reduced toxicity compared to $Gd^{III}$ analogues. In addition, the MCE has been observed in $Mn^{II}$ systems, taking advantage of the small magnetic anisotropy.[23−26]

While the stereochemistry of six-coordinate coordination compounds is typically dominated by the octahedron or *pseudo*-octahedron, other geometries such as trigonal prismatic are also possible. Although trigonal prismatic geometry is somewhat of a rarity,[27−29] it is relatively well-known in $Mn^{II}$, where the isotropic half-filled d-subshell, means it is coordinatively less demanding than other $d^n$ configurations where trigonal prismatic geometry can be conferred by use of

**Received:** November 15, 2025
**Revised:** February 20, 2026
**Accepted:** March 11, 2026
**Published:** March 18, 2026

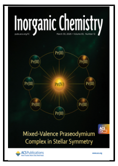

strained ligands.[30−36] Siting $Mn^{II}$ in a strained coordination environment offers a good opportunity to probe how this will affect the electronic structure which is often reported as highly isotropic regardless of shape.[2,10]

Typically, in order to confer trigonal prismatic geometry a relatively rigid ligand framework is required, such as that offered by macrocyclic,[30−32] tripodal,[37−39] or encapsulating ligands.[33−36] We now report a new series of $Mn^{II}$ complexes with an acyclic hexadentate Schiff base ligand framework which readily confers trigonal prismatic geometry as measured by Continuous Shape Measures (CShM), but where EPR spectroscopy over a range of field strengths and frequencies reveals an almost perfectly rhombic electronic arrangement. The employed ($R$-sal$_2$pipz) ligand, derived from two salicylaldehydes ($R$-sal) and 1,2-bis(3-aminopropyl)piperazine (pipz), has been shown to be sufficiently rigid to support distorted trigonal prismatic geometry in $Co^{II}$ ($d^7$ high-spin),[40,41] $Mn^{III}$ ($d^4$ high-spin),[42] and $Fe^{III}$ ($d^5$ high-spin).[43] Nevertheless, the general ligand type also proves to be flexible in some cases, Figure S1.1, stabilizing a distorted octahedron in $Co^{III}$ ($d^6$ low-spin),[42,44−46] for which trigonal prismatic geometry would be significantly unfavorable due to a large Ligand Field Stabilization Energy (LFSE) preference for the octahedral geometry. We report here nine new examples of this ligand framework with $Mn^{II}$, Table 1, where the CShM suggests a trigonal prismatic geometry.

**Table 1. Summary of Continuous Shape Measures (CShM) and Selected Structural Distortion Parameters for 1−9**

| complex | CShM (TPR) | CShM (OC) | $\tau_{avg}$ (°) | $\eta$ (°) |
|---|---|---|---|---|
| **1** [$Mn^{II}$(3-$NO_2$-sal$_2$pipz)] | 0.826 | 15.822 | 2.5 | 2.12 |
| **2a** [$Mn^{II}$(3-$NO_2$-5-OMe-sal$_2$pipz)] | 0.779 | 15.417 | 3.5 | 1.08 |
| **2b** [$Mn^{II}$(3-$NO_2$-5-OMe-sal$_2$pipz)] | 0.796 | 14.743 | 4.6 | 1.40 |
| **3a** [$Mn^{II}$(3-$NO_2$-5-Cl-sal$_2$pipz)] | 1.176 | 12.528 | 9.6 | 1.88 |
| **3b** [$Mn^{II}$(3-$NO_2$-5-Cl-sal$_2$pipz)] | 1.049 | 13.960 | 6.4 | 2.54 |
| **4** [$Mn^{II}$(3-Br-5-$NO_2$-sal$_2$pipz)] | 0.903 | 13.640 | 6.9 | 1.17 |
| **5** [$Mn^{II}$(3-OMe-5-$NO_2$-sal$_2$pipz)] | 1.034 | 12.944 | 8.4 | 1.07 |
| **6** [$Mn^{II}$(5-$NO_2$-sal$_2$pipz)] | 1.167 | 12.441 | 9.7 | 1.37 |
| **7** [$Mn^{II}$(3,5-diCl-sal$_2$pipz)] | 1.058 | 13.364 | 7.7 | 1.70 |
| **8** [$Mn^{II}$(3,5-diBr-sal$_2$pipz)] | 1.042 | 13.128 | 8.3 | 2.05 |
| **9** [$Mn^{II}$(3,5-diI-sal$_2$pipz)] | 1.036 | 13.118 | 8.3 | 1.22 |

Although the ligand framework is important, additional consideration of the electronic configuration of the given metal is required. Wentworth utilized LFSE to predict the relative stability of both the octahedron (OC) and trigonal prism (TPR) for all $d^n$ configurations.[47] The LFSEs for the idealized OC ($O_h$) and TPR ($D_{3h}$) are equal for the $d^0$, $d^1$, $d^2$ (low-spin TPR), $d^5$ (high-spin), $d^6$ (high-spin) or $d^{10}$ electronic configurations, and, as such, there is no electronic preference of geometry, Figure 1. On the contrary, $d^3$ (high-spin), $d^6$ (low-spin) or $d^8$ (low-spin) are unlikely to support the TPR geometry due to the greater LFSE of the octahedral geometry, Figure 1. Alvarez et al. used density functional theory to calculate the relative energy differences along the Bailar pathway between the octahedron and trigonal prism for $[M(tacn)_2]$ complexes, where tacn = 1,4,7-triazacyclononane.[27] The results reveal that the octahedron is generally more energetically favorable (except for $d^0$ and $d^1$), but the energy difference is smaller for those configurations with no preference due to LFSE (high spin $d^5$, $d^{10}$), hence the relative prevalence of high spin $Mn^{II}$ complexes with trigonal prismatic geometry. Here we show that the combination of a half-filled d-subshell and the trigonal environment provided by the ligand yields $S = 5/2$ systems exhibiting a maximally rhombic ZFS ($E/D = 0.33$).

## ■ EXPERIMENTAL SECTION

Details of the syntheses of **1**−**13** are provided in section S1 of the Supporting Information. Elemental analysis (C, H, N) was performed on polycrystalline samples using an Exeter Analytical CE-440 Elemental Analyzer. Infrared spectra were recorded on polycrystalline samples of **1**−**13** using a Bruker ALPHA Platinum ATR-FTIR spectrometer fitted with a diamond anvil. UV−visible spectroscopy was carried out both in solution and in the solid state, using an Agilent Cary 60 UV−visible spectrometer. Magnetic measurements were performed using a Quantum Design MPMS-XL SQUID magnetometer operating between 2 and 300 K.

Single crystal X-ray diffraction (SCXRD) was performed on crystals of **1**−**13** using a Rigaku Oxford Diffraction SuperNova diffractometer with an Atlas CCD detector. Data were collected at 100 K with the temperature controlled using an Oxford Instruments Cryojet. Data were collected using either Mo K$\alpha$ radiation (0.71073 Å) or Cu K$\alpha$ radiation (1.54184 Å). *CrysAlis$^{PRO}$* software was used for the data collection, integration, reduction and finalization.[48] An analytical absorption correction based on the shape of the crystal along with an empirical absorption correction was performed in CrysAlis$^{PRO}$.[49] Structures were solved using direct methods with ShelXS[50] or ShelXT[51] and refined by full matrix least-squares on $F^2$ with ShelXL.[52] Hydrogen atoms were geometrically constrained and refined riding on the parent atom. Complex **1** was refined as a two-component inversion twin with a ratio of 0.508(13):0.492(13) of each component. Further crystallographic details for **1**−**13** are included in Table S2.1. The structures for **1**−**13** have been deposited in the Cambridge Structural Database (CSD) with deposition numbers CCDC-2410990−2411004. These can be obtained free of charge from The Cambridge Crystallographic Data Centre via www.ccdc.cam.ac.uk/structures

The analysis of the relative abundance of the trigonal prismatic geometry in structures published in the CSD[53] was carried out using the ConQuest program.[54] At the time of searching (December 2024 Update) there was a total of 1,331,521 entries in the CSD. In order to narrow the search, only entries containing hexacoordinate manganese(II) sites with nonmetal atom donors were considered. Of the ~1.3 million entries in the CSD, 28,061 entries contained manganese, of this 18,682 were six-coordinate with nonmetal donor atoms, of these 7,409 had the oxidation state assigned as only $Mn^{II}$. Not all structures in the CSD, however, have the oxidation state assigned and there are also some entries which have more than one manganese site each with different oxidation states. In order to assign the oxidation state of the unassigned structures, and those of individual sites in multinuclear structures with more than one oxidation state assigned, we utilized bond valence sum (BVS).[55] The oxidation state of the atom of interest can be determined using the equation

$$V_i = \sum_j s_{ij} = \sum_j \exp\left(\frac{R_0 - R_{ij}}{B}\right)$$

where $V_i$ is the oxidation state of atom $i$ (in this case, Mn), $s_{ij}$ is the bond valence between atoms $i$ and $j$, $R_0$ is the "ideal" bond length for a given atom pair, $R_{ij}$ is the experimental bond length between atoms $i$ and $j$, and $B$ is an empirical constant (in most cases, as here, 0.37). The empirical values for $R_0$ have been reported for many Mn-ligand combinations.[56] Utilizing this method we identify a further 8,110 $Mn^{II}$ sites from the unassigned structures and from sites in structures with more than one oxidation state described. This gives a total of 18,049 $Mn^{II}$ sites which we then analyzed using Continuous Shape Measures (CShM) using the SHAPE program.[57] Further details are provided in Section S2.4 in the Supporting Information.

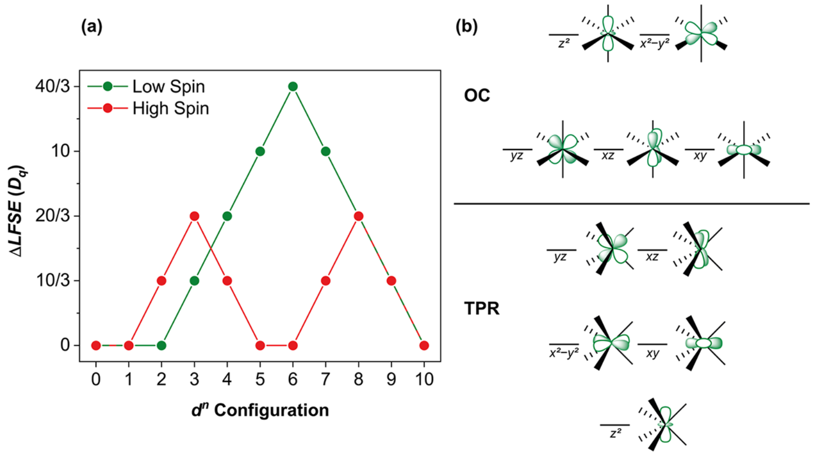

**Figure 1.** (a) Deviation in the value of $\Delta LFSE$ for $d^n$ electronic configurations from $d^0$ to $d^{10}$, where $\Delta LFSE = LFSE(\mathrm{OC}) - LFSE(\mathrm{TPR})$. Those points with zero value have no electronic preference between OC and TPR, whereas those with increasing values of $\Delta LFSE$ have a greater preference for OC. The red and green points represent high spin and low spin configurations, respectively, where applicable. (b) Splitting diagram of the *d*-orbitals for the idealized OC ($O_h$ symmetry) and TPR geometry ($D_{3h}$ symmetry).

X-band EPR spectra were recorded on a frozen solution and powder of **1** using a Magnettech MS200 spectrometer fitted with a liquid nitrogen dewar. The samples were prepared in a solution of dichloromethane and toluene (1:1) at a ~20 mM concentration. Continuous-wave high-field EPR (cw-HFEPR) measurements were performed at the National High Magnetic Field Laboratory (NHMFL, Tallahassee, Florida) using a homodyne transmission spectrometer[58] equipped with a superconducting magnet and a helium flow cryostat (Oxford Instruments plc, UK), allowing for variable temperature studies in magnetic fields up to 14.5 T. Measurements were carried out on pressed powder samples of **1** and **6**, and a frozen solution of **1** (dichloromethane and toluene, 1:1). Spectra were recorded at multiple frequencies in the 50 to 600 GHz range, generated using a phase-locked microwave source with a base frequency of 13.1 ± 1 GHz followed by a solid-state harmonic multiplier chain (Virginia Diodes Inc., Charlottesville, VA). Field-modulated derivative-mode EPR signals were detected using a helium-cooled InSb bolometer (QMC Ltd., Cardiff, UK) and recorded using a lock-in amplifier (Stanford Research Systems, Sunnyvale, CA).

## ■ RESULTS AND DISCUSSION

### Continuous Shape Measure (CShM) Analysis

First, in order to quantify the prevalence of the TPR geometry in six-coordinate $Mn^{II}$ complexes, a survey of published crystal structure data in the Cambridge Structural Database (CSD) was performed. Of the 28,061 CSD entries containing manganese, there are 18,682 with six-coordinate manganese sites with nonmetal donor atoms. Many of these CSD entries constitute polynuclear complexes, so of the 18,682 unique entries there are 31,483 unique manganese sites. Of these 31,483, we identified 18,049 $Mn^{II}$ sites where the oxidation state is either explicitly assigned in the CSD or where we have determined the oxidation state using Bond Valence Sum (BVS). Continuous Shape Measure (CShM)[59−61] was used to quantitatively define the coordination geometry of all the six-coordinate $Mn^{II}$ centers. A plot of the CShM for the ideal octahedral (OC) and trigonal prismatic (TPR) geometries is presented in Figure 2. As most structures adopt an intermediate geometry between octahedral and trigonal prismatic, two additional parameters are considered, $\Delta_{\mathrm{OC,TPR}}$ and $\psi_{\mathrm{OC,TPR}}$, as defined previously by Alvarez et al.[27,47,62,63] The minimum distortion pathway between the octahedral and trigonal prismatic geometry, known as the Bailar pathway,[29] is used to define these parameters. The path deviation function, $\Delta_{\mathrm{OC,TPR}}$, quantifies the deviation of a geometry from the Bailar pathway, and the generalized interconversion coordinate, $\psi_{\mathrm{OC,TPR}}$, gives the percentage conversion from the ideal octahedral to trigonal prismatic geometry, whereby $\psi_{\mathrm{OC,TPR}}$ = 100% would indicate full conversion to the TPR geometry along the Bailar pathway. Only 2.1% of all $Mn^{II}$ sites with six-coordinate nonmetal donor atoms exhibit mostly trigonal prismatic geometry, whereas the vast majority, 76.4%, can be considered to be mostly octahedral. We define structures as mostly TPR (or OC) if the respective CShM is less than 3. In order to better understand the typical ligands in the CSD

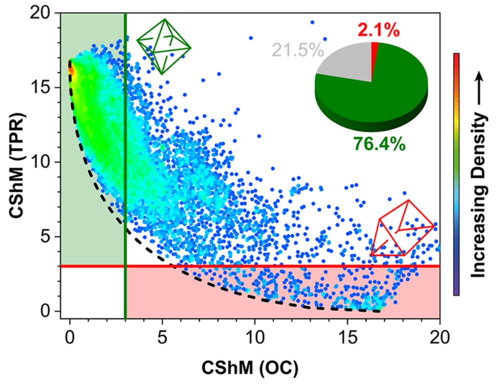

**Figure 2.** Density plot of the abundance of structures in the CSD containing a six-coordinate $Mn^{II}$ site with nonmetal donor atoms, plotted as CShM for the trigonal prismatic (TPR − *y*-axis) geometry versus the octahedral (OC − *x*-axis) geometry. Each point represents a $Mn^{II}$ site identified in the CSD, with the color scale representing the relative degree of overlap of the points (*i.e.* red coloring indicates a higher density of overlapping points compared to green and blue). The vertical green line at CShM(OC) = 3 represents the cutoff point for the geometry to be considered *mostly* octahedral, the horizontal red line represents the equivalent for trigonal prismatic. The dashed black line represents the Bailar pathway. *Inset:* Percentage abundance of each type of geometry: octahedral (green), trigonal prismatic (red), others (gray). A $Mn^{II}$ site is considered *mostly* octahedral (OC) or trigonal prismatic (TPR) if the respective CShM values are less than 3, as per the cutoff point in the main plot, i.e., those in the red shaded area can be considered trigonal prismatic and those in the green shaded area octahedral.

**Scheme 1. Generic Route For Synthesis of Complexes 1−9**[a]

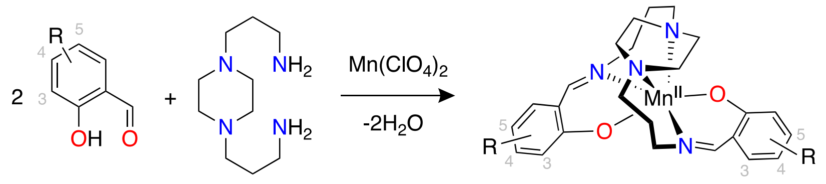

[a] The numbering on the phenolate rings is used to describe the functional group substitution of the ligand.

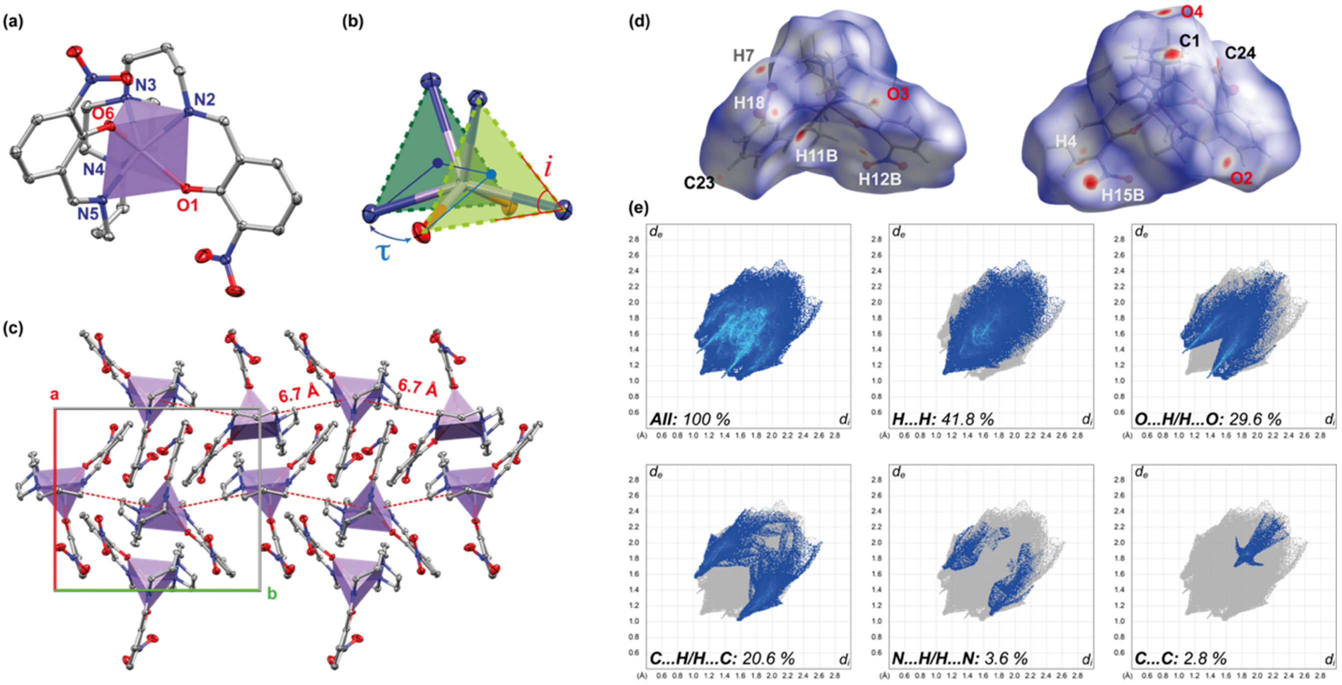

**Figure 3.** (a) Asymmetric unit of **1**. (b) Illustration of the $\tau$ and $i$ angles considered in this paper, where $\tau_{avg}$ is the average of the three torsional angles between the two atoms at either end of a side of the trigonal prisms and the centroids of each triangular face (sometimes referred to as the Bailar twist angle), and $\eta$ is the average deviation from 60° of the six angles $i$ of the top and bottom triangular faces. (c) Packing diagram of **1** showing the chain formation with 6.7 Å interatomic distance between the Mn centers. (d) Two views of the Hirshfeld surface of **1** mapped over $d_{\text{norm}}$ in the range of −0.1511 to 1.5840 au, where the atom labels indicate intermolecular contacts with atoms outside of the surface. (e) Two-dimensional fingerprint plots for **1** sorted into the main atom combinations. The percentage of the surface coverage is indicated. The O···H/H···O fingerprint plot reveals the presence of intermolecular C−H···O hydrogen bonding with the nitro groups on the phenolate ring.

which support the TPR geometry, the corresponding 378 sites (representing the 2.1%) were surveyed, Table S2.10. Most of the entries with TPR geometry were obtained using rigid encapsulating ligands, macrocycles or were part of a larger multimetal cluster. Only 72 sites (0.4% all Mn$^{II}$ sites) had a mononuclear Mn$^{II}$ center with a mostly TPR geometry, Table S2.10. In fact, only one entry was reported with a hexadentate open chain ligand, 1,10-bis(2-pyridylmethyl)-1,4,7,10-tetraazadecane.[64]

## Synthesis

We utilize a hexadentate Schiff base ligand to encapsulate the Mn$^{II}$ center in this work, and nine complexes, Table 1, were synthesized through a facile one-pot Schiff base condensation followed by complexation around a Mn$^{II}$ center, Scheme 1. The addition of an electron withdrawing group (EWG) as a substituent on the salicylaldehyde ring was used to prevent aerial oxidation to Mn$^{III}$, as stabilization of Mn$^{II}$ with EWG substituted Schiff base ligands has been observed in the literature.[65] Weakly inductive EWGs, such as halo-substituents, were sufficient for stabilization of the +2 oxidation state, along with the stronger nitro group, all of which are air stable over a number of years.

## Single Crystal X-ray Diffraction

Single crystal X-ray diffraction (SCXRD) was used to characterize the structures of **1** − **9**. Complex **1** crystallizes in the noncentrosymmetric $P2_12_12_1$ space group as an inversion twin with around 50% of each component. The asymmetric unit of **1** is shown in Figure 3(a). We identified the presence of two polymorphs of **2** in separate batches, one in the centrosymmetric $I2/a$ space group (**2a**) and the other in the noncentrosymmetric $Fdd2$ space group (**2b**), both with internal $C_2$ axes, Table S2.2. Complex **3** also crystallizes as two polymorphs; however, in this case, they were easily distinguished. Bright-orange needles crystallize almost immediately, which we identified as a triclinic $P\bar{1}$ phase (**3a**) and, over time, if the solution is left standing, these redissolve and deep red-orange blocks form, which we identified as a monoclinic $P2_1/n$ phase (**3b**). Complexes **4**−**8** crystallize in the centrosymmetric $C2/c$ ($I2/a$) space group, with half of the molecule in the asymmetric unit ($Z$ = 4, $Z'$ = 0.5), bisected by a 2-fold rotational axis. Finally, **9** crystallizes in the triclinic $P\bar{1}$

space group. Further crystallographic information can be found in Tables S2.1 and S2.2.

In **1−9** the structures consist of a $Mn^{II}$ center bound by the hexadentate ligand with an $N_4O_2^{2-}$ coordination sphere, which adopts a trigonal prismatic geometry. Selected bond lengths and angles are presented in Table S2.2. The average bond lengths for the Mn−O, $Mn-N_{imine}$ and $Mn-N_{amine}$ contacts are 2.0984(14) Å, 2.2593(17) Å and 2.3327(17) Å, respectively, which are all within the range of expected bond lengths for $Mn^{II}$. The 1,4-piperazine ring in the backbone of the ligand adopts a boat conformation, as opposed to the more energetically favored chair conformation, which is normally adopted in the absence of a metal.[41,66] Complex **1** shows an almost ideal boat conformation of the 1,4-piperazine ring, with N−C−C−N torsion angles of 2.7(2)° and 4.4(2)°. Cremer-Pople analysis[67,68] confirms the almost ideal boat conformation of the piperazine ring. For **1**, the ring puckering amplitude is $Q$ = 0.832(2) Å, and the two angular variables are $\theta = 90.72(14)°$ and $\phi = 3.34(17)°$. A value of $\theta = 90°$ and $\phi = 0$ or 180° would be expected for an ideal boat confirmation. The constrained nature of the piperazine ring in the backbone results in the N3−Mn−N4 angle of 65.02(6)° being significantly smaller than that of the N2−Mn−O1 and N5−Mn−O6 angles of 81.97(6)° and 80.98(6)°, respectively, though not dissimilar to other complexes of the ($R$-$sal_2$pipz) ligand.[40−43] This smaller N3−Mn−N4 "bite" angle results in a tilting of the triangular faces of the trigonal prism of $\delta = 7.2°$. As a result, the $Mn^{II}$ atom sits off-center in the trigonal prism, giving rise to the longer $Mn-N_{amine}$ distances. Structurally, all the complexes **2−9** are very similar to **1**, with slight distortions to the coordination sphere upon varying the ligand substitution. The only major difference is the angle, $\alpha$, between the planes of the phenolate rings, which varies widely between **1−9**. The respective maximum and minimum $\alpha$ angles are 102.6° for **9** and 164.4° for **2b**, with a value of 119.3° for **1**. Despite these variations, the $\alpha$ angle does not appear to dictate whether the site is more trigonal prismatic which is more likely due to a combination of the relative stability of a given ligand and the effect of packing in the lattice. In order to describe the coordination geometry, we define two other parameters (Figure 3(b) and Table 1): $\tau$ is the torsion angle between the top and bottom triangular faces of the trigonal prism (sometimes termed the Bailar twist angle) where a value of 0° would represent a perfect trigonal prism; $\eta$ is the deviation from 60° of each angle in the triangular faces at the top and bottom of the trigonal prism, defined by eq 1

$$\eta = \frac{1}{6}\sum_{i=1}^{6} |60 - i| \qquad (1)$$

For **1**, the values of $\tau = 2.5°$ and $\eta = 2.12°$ are obtained, both of which are close to ideal. The $\eta$ values for **1−9** do not deviate greatly, ranging from 1.07° (**5**) to 2.54° (**3b**). In general, the $\tau$ value increases as the geometry becomes less trigonal prismatic, with **1** having the lowest value and **6** the highest value of $\tau = 9.7°$. A further summary of the structural analysis and parameters for **1−9** is given in Tables S2.2 and S2.3.

In complex **1**, crystal packing results in chains of molecules parallel to the $b$-axis, with a Mn−Mn interatomic distance of 6.67 Å, Figure 3(c), we do not expect intermetallic magnetic interactions at this distance. Although there is no classical hydrogen bonding in **1**, some intermolecular C−H···A (A = acceptor) bonding interactions are present, most notably C−H···O interactions with the oxygen of the nitro group acting as a hydrogen bond acceptor. The intermolecular interactions are summarized in Table S2.5. In order to obtain more information about intermolecular interactions, we performed Hirshfeld surface analysis[69,70] using the CrystalExplorer software.[71] The Hirshfeld surface of **1** is dominated by H···H van der Waals interactions, which account for 41% of the surface area, followed by O···H interactions (29.6%), which include the C−H···O interaction discussed previously. The Hirshfeld surface for **1** is shown in Figure 3(d) with major contacts indicated, along with 2D fingerprint plots delineated into the major atom combinations in Figure 3(e). Complexes **1−9** have varying degrees of other interactions which are shown in Figures S2.4−S2.13, and in those complexes where halogens are present in the ligand (**3**, **4**, **7−9**), C−X···H, C−X···C and X···X (where X is the halogen) interactions replace the C−H···O interactions. The relative percentage of Hirshfeld surface for **1−9** is shown in Figure S2.14 and summarized in Table S2.6.

Continuous shape measure (CShM) was used to further probe the coordination geometry around the $Mn^{II}$ centers, and the results are summarized in Table 1 and Figure 4. The CShM measure reveals that complex **2a** has the most trigonal prismatic geometry, with both polymorphs having CShM(TPR) < 0.8, with **3a** being the least trigonal prismatic, with CShM(TPR) = 1.176. All complexes do, however, fall well below the cutoff stated earlier for defining the geometry as trigonal prismatic. All of the complexes have a significant deviation from the Bailar pathway ($\Delta_{OC,TPR}$ > 10%) which is not surprising given the tilt of the triangular faces of the prism. As such, the generalized coordinates ($\psi_{OC,TPR}$) along the Bailar pathway, Table S2.2, are not reliable due to the large deviation from the pathway.

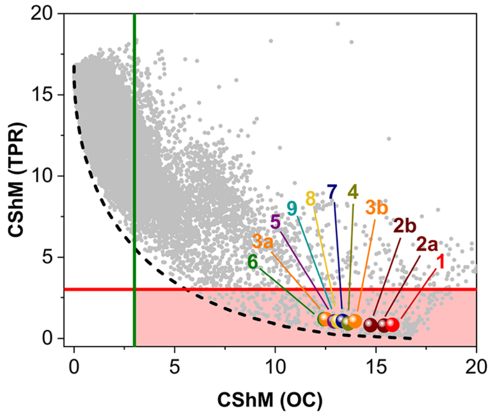

**Figure 4.** CShM plot for **1−9** (colored spheres) with CShM(OC) on the $x$-axis and CShM(TPR) on the $y$-axis, as in Figure 2. The vertical green line at CShM(OC) = 3 represents the cutoff point for the geometry to be considered mostly octahedral, the horizontal red line represents the equivalent for trigonal prismatic. Those points in the red shaded area can be considered trigonal prismatic. The dashed black line represents the Bailar pathway. The gray points represent all $Mn^{II}$ sites from the CSD (as per Figure 2).

## Magnetic Measurements

Magnetic measurements were performed on polycrystalline samples of **1** and **6**. A magnetic susceptibility−temperature product, $\chi_M T$ = 4.30 $cm^3$ K $mol^{-1}$, is obtained for **1** at room temperature, in agreement with the spin-only value for high-

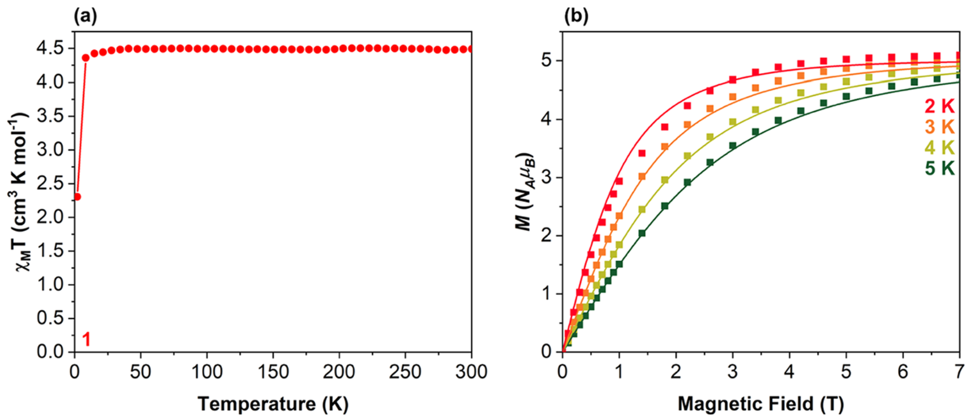

**Figure 5.** (a) Magnetic susceptibility−temperature product ($\chi_M T$) recorded between 3 and 300 K (left). The experimental data is represented by the red points, with the line connecting the points a guide for the eye. (b) Magnetization versus magnetic field ($M$ *vs* $\mu_o H$) at 2, 3, 4, 5 K (right) for **1**. The squares represent the experimental data points, and the lines represent simulations based on the spin Hamiltonian parameters deduced from high-field and -frequency EPR measurements.

spin (HS, $S = 5/2$) Mn$^{II}$ of 4.38 cm$^3$ K mol$^{-1}$. The same is found consistently across the measured temperature range (300−3 K), Figure 5(a), apart from a sharp decrease at the lowest temperatures, which is attributed to zero-field splitting. The field-dependent magnetization ($M$ *vs* $\mu_o H$) was measured at 2, 3, 4, and 5 K between 0 and 7 T, Figure 5(b). The experimental data points lie close to the simulated curves, which were generated using the EasySpin program,[72] with the spin Hamiltonian of eq 2 and the parameters obtained from high-field and -frequency EPR (HF-EPR, *vide infra*).

## Electron Paramagnetic Resonance Spectroscopy

To further understand the electronic structure and the nature of any potential zero-field splitting (ZFS) interactions for these complexes, electron paramagnetic resonance (EPR) spectroscopy was performed. For HS Mn$^{II}$, with total spin $S = 5/2$, the electronic properties can be described by the following effective spin Hamiltonian

$$\hat{\mathcal{H}} = \mu_B g \mathbf{B}\cdot\hat{S} + A\hat{I}\cdot\hat{S} + D\left[\hat{S}_z^2 - \frac{1}{3}S(S+1)\right] + E(\hat{S}_x^2 - \hat{S}_y^2) \quad (2)$$

The first term denotes the Zeeman interaction assuming an isotropic $g$-factor close to the free-electron value (2.0023), as is typical for the HS d$^5$ electronic configuration; the second term parametrizes the hyperfine interaction involving the $I = 5/2$ $^{55}$Mn nuclear magnetic moment, again assuming an isotropic coupling constant, $A$; the last two terms represent the axial and rhombic ZFS interactions, parametrized respectively by $D$ and $E$; $\hat{S}$ is the total spin operator with components $\hat{S}_i$ ($i = x, y, z$) and $\mu_B$ is the Bohr magneton.[2,10,73] The ZFS interaction is typically weak ($|D| < 1$ cm$^{-1}$, with $|E| \leq |D|/3$) for the HS d$^5$ electronic configuration (i.e., Mn$^{II}$).[10,73] Nevertheless, when utilizing X-band EPR (9.4 GHz, 0.3 cm$^{-1}$), one often only observes a sextet centered at $g^{eff} = 2.00$ (330 mT), representing the central transition from $m_s = -1/2$ to $+1/2$, which is then split into six lines due to the hyperfine interaction with the $I = 5/2$ $^{55}$Mn nucleus.

The X-band EPR spectrum of **1**, recorded for a frozen glass (77 K, dichloromethane/toluene, 1:1), is shown in Figure 6. An intense multiline signal is observed between 120−200 mT (centered around $g^{eff} \approx 4.3$), attributable to several overlapping resonances, along with a broad signal centered at 330 mT ($g^{eff} = 2$) and a weak sextet centered at 70 mT ($g^{eff} \approx 9.8$).

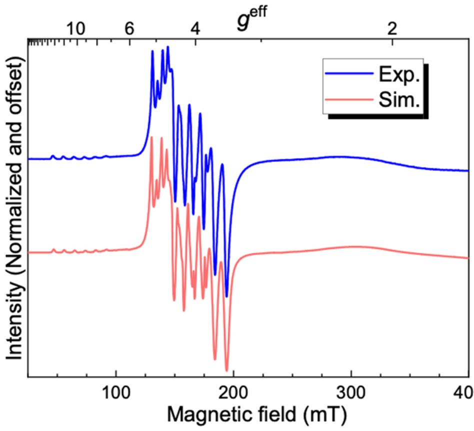

**Figure 6.** Experimental (Exp.) X-band (9.38 GHz) EPR spectrum of **1** recorded at 77 K in a frozen glass (dichloromethane/toluene, 1:1), shown together with the best simulation (Sim.); the experimental spectrum was recorded in derivative mode, yielding the field-modulated intensity. The simulations are more-or-less insensitive to the absolute values of the ZFS parameters $D$ and $E$, although they are sensitive to the ratio $E/D$. For this reason, initial values of $D$ and $E$ were taken from the high-field and -frequency measurements, then $A^{iso}$, $g^{iso}$, and $E/D$ were varied to obtain the best simulation, with the optimum parametrization given in Table 2; a peak-to-peak Lorentzian line width of 0.5 mT together with 12.5% strains in both $D$ and $E$ were employed in the simulations.

Hyperfine splitting ($^{55}$Mn $I = {}^5/_2$) is observed in both the $g^{eff} = 4.3$ and 9.8 signals, with simulations (*vide infra*, see Table 2) indicating a value of $A^{iso} = 250$ MHz ($\equiv$ 89.3 G). The spectrum is somewhat atypical for Mn$^{II}$, although exactly as expected for a near maximally rhombic ($E = D/3$) system with the high-spin d$^5$ electronic configuration.[74] For example, a powder spectrum recorded on the TPR [Mn$^{II}$(acac)$_2$(bpy)] complex has previously been reported by van Gorkum et al., where a broad resonance centered at $g^{eff} = 4.3$ is observed,[75] and a similar spectrum has been recorded on a powder sample of K[Cd(Mn$^{II}$)(acac)$_3$] by Goodgame and Birdy.[76] Likewise, we observe a broad resonance centered at $g^{eff} = 4.3$ and a further broad resonance at $g^{eff} = 2$ when performing measurements on a powder of **1**, Figure S3.1. Powder spectra are often broadened due to intermolecular dipole−dipole interactions as well as $D$-strain, making it difficult to observe

**Table 2. Summary of Spin Hamiltonian Parameters [see Eq. 2] Obtained through Simulation of the Multi-High-Frequency EPR Spectra for 1 and 6**

| | $g_x$ | $g_y$ | $g_z$ | $A^{\text{iso}}$ (MHz) | $D$ ($\text{cm}^{-1}$)[a] | $E/D$ | $B_4^3$ |
|---|---|---|---|---|---|---|---|
| | | | **1** [$\text{Mn}^{\text{II}}$(3-$\text{NO}_2$-$\text{sal}_2$pipz)] | | | | |
| X-band EPR Frozen Glass | 2.000 | 2.000 | 2.000 | 250 | +0.200[b] | 0.305[c] | |
| HF-EPR Frozen Glass | 2.000 | 2.000 | 2.000 | 242 | ±0.200 | 0.333 | |
| HF-EPR Powder | 1.990 | 1.985 | 1.990 | | ±0.200 | 0.333 | ±0.032[d] |
| | | | **6** [$\text{Mn}^{\text{II}}$(5-$\text{NO}_2$-$\text{sal}_2$pipz)] | | | | |
| HF-EPR Powder | 1.990 | 2.000 | 2.000 | | ±0.230 | 0.333 | ±0.020[d] |

[a] In the rhombic limit ($E = D/3$), the sign of $D$ is undetermined and has no meaning, i.e., both positive and negative parametrizations give identical simulations and identical Zeeman level diagrams. [b] The positive parametrization was used in simulating the spectra, but it is virtually indistinguishable from the negative one due to the fact that this is still close to the rhombic limit. [c] The $D$ parameter was set to the value obtained at high frequencies and only the $E/D$ ratio was varied during the simulations. [d] Simulations are insensitive to the sign of $B_4^3$.

finer details including hyperfine splitting. In frozen solution, however, van Gorkum et al. observe the typical $\text{Mn}^{\text{II}}$ resonance centered at $g^{\text{eff}} = 2$ for the [$\text{Mn}^{\text{II}}(\text{acac})_2(\text{bpy})$] complex, suggesting the complex adopts a more octahedral geometry in solution.[75]

The sharp hyperfine features observed in the X-band spectrum arise from transitions within the three Kramers doublets associated with the electronic sextet. These transitions are allowed in complex **1** due to a highly rhombic ZFS tensor, and this is also the reason for the atypical effective *g*-values of 4.3 and 9.8. However, even though the ZFS tends to be weak for the $S = 5/2$ $d^5$ configuration, it is appreciable enough in complex **1** (and **6**, *vide infra*) that one cannot clearly observe the inter-Kramers transitions that would constrain $D$ and $E$ (the zero-field gaps between Kramers doublets are of the order of 20 GHz). Therefore, it becomes necessary to utilize higher field and frequency measurements in order to gain insight into the ZFS parameters. In particular, the condition $h\nu \gg |D|$ ensures easy interpretation of the EPR spectra, as the $m_s$ sublevels become pure and separate linearly with magnetic field. To this end, both **1** and **6** were investigated using HF-EPR. Although **2a** is the most trigonal prismatic and **3a** the least, we chose not to study these samples due to the evidence of polymorphism in the batches, instead selecting **1** as the most trigonal prismatic with no polymorphs and **6** as the least trigonal prismatic with no polymorphs. Spectra were recorded at multiple frequencies between 50 and 500 GHz within the 0−14.5 T magnetic field range. The multifrequency powder and solution EPR spectra were then simulated to parametrize the effective spin Hamiltonian in eq 2, as shown in Figure 7.

Figure 7(a) shows selected low-temperature (~7 K) HF-EPR spectra for **1** in a frozen glass (dichloromethane/toluene, 1:1). Each spectrum is plotted relative to the central $g_c = 2.00$ position, $B_c = hf/g_c\mu_B$, to aid in viewing and for the purposes of comparing the fine structures observed at each frequency. Simulations are also shown below each experimental spectrum; the complete data set, plotted with respect to applied field, can be seen in Figure S3.2. A strong central feature is observed at all frequencies, corresponding to transitions within the $m_S = \pm 1/2$ Kramers doublet. These transitions do not experience any first-order ZFS, which is why they occur close to the $g_c = 2$ position with narrower line widths due to insensitivity to $D$-strain. Moreover, second-order ZFS effects increase with applied magnetic field, leading to a further narrowing of the central transitions and excellent resolution of the hyperfine coupling, as illustrated for the highest frequency spectrum in the upper-right inset, Figure 7.

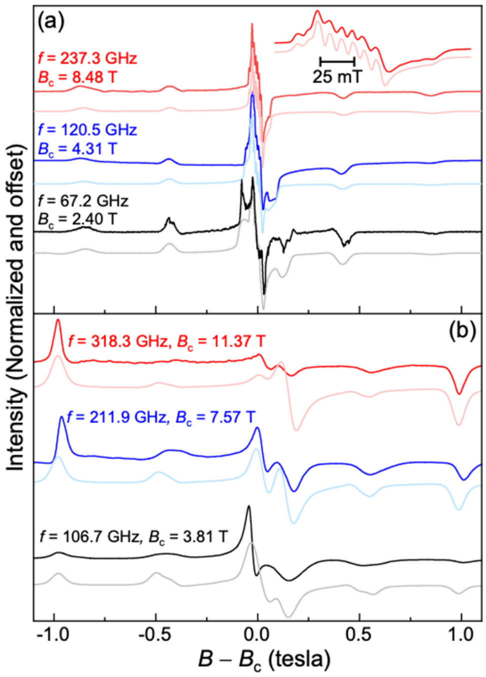

**Figure 7.** Selected derivative-mode HFEPR spectra (dark traces) and simulations (light traces) for: (a) a frozen solution of **1** (dichloromethane/toluene, 1:1), and (b) a polycrystalline powder of **6**, recorded at ~ 8 K and plotted as a function of $B{-}B_c$, where $B_c$ is the $g = 2.0$ position; see legend for frequencies and associated $B_c$ values. The simulations for **1** employed 12% strains in both $D$ and $E$ and a 2 mT Lorentzian peak-to-peak line width, while those for **6** employed a mixture of $D$ and $E$ strain (2% and 1%, respectively), with more substantial Lorentzian (25 mT) and Gaussian (40 mT) peak-to-peak line widths.

Weaker features (peaks/dips) are seen either side of the central transitions in Figure 7(a), at positions that do not vary with field/frequency (when plotted versus $B{-}B_c$), confirming that the observed splitting pattern is due to the field-independent ZFS interactions, $D$ and $E$ [eq 2], and not due to $g$-anisotropy. These features are attributed to inter-Kramers transitions (e.g., $m_S = -\frac{5}{2} \rightarrow -\frac{3}{2}$) which are first-order sensitive to $D$-strain (disorder). This leads to increased line widths and weaker intensities in derivative mode, such that the hyperfine splitting is unresolved in all but the central transition. For this reason, $D$ and $E$ strains are included in the simulations in order to capture the broadening of the outer peaks, while the intrinsic peak-to-peak line width reflected in the central transition is rather narrow [2 mT, see inset to Figure 7(a)]. In fact, there is a 4-fold increase in the peak-to-peak line width used in the simulations at 237.3 GHz relative to those at X-band, likely reflecting effects of *g*-strain observed at the higher fields/frequencies. In general, five electronic transitions are expected within the HS $d^5$ sextet for each component of the *D*-tensor and in the absence of rhombicity, the fine structure peaks would be weighted more toward one or other side of the central position, depending on the sign of *D*. However, in the case of **1** (and **6**, *vide infra*) a central transition is observed with two broad peaks/dips equally spaced on either side. This splitting pattern is characteristic of a maximally rhombic spectrum ($E = D/3$), with overlapping equally spaced peaks/dips for each component of the *D*-tensor, thus confirming the initial conclusions of the X-band measurements.[2]

Interestingly, the best simulations of the X-band and high-field and -frequency solution EPR spectra for **1** result in slightly different spin Hamiltonian parameters (Table 2), even though the same solvent mixture was employed for both measurements. We speculate that this is due to the different temperatures employed (77 K versus ~7 K). In particular, $A^{\mathrm{iso}}$ decreases slightly from 250 to 242 MHz upon cooling, while $E/D$ increases from 0.305 at 77 K to the maximum of 0.33 at 8 K. Meanwhile, simulations of HF-EPR measurements on a powder sample of **1** (Figures S3.3 and S3.4) give very similar ZFS parameters to the solution samples, with the additional inclusion of fourth-order interaction (see below and Table 2). The outermost peaks/dips seen in the powder spectra of **1** are again equidistant from the central transition, consistent with a highly rhombic $Mn^{II}$ species ($E = D/3$), suggesting that **1** adopts a similar structure in solution and the solid state. These findings support the idea that it is the ligand that enforces the coordination geometry, which does not change significantly between solution and solid-state forms. No hyperfine splitting is resolved due to the high spin concentration of the solid-state samples, which leads to appreciable spin−spin dipolar line broadening.

Compound **6** was insufficiently soluble to perform measurements on a frozen solution. Therefore, EPR studies were limited to a powder sample [Figures 7(b) and S3.5]. Similar to the powder of **1**, hyperfine splitting patterns are not resolved due to the high spin concentration. Nevertheless, field-independent fine structures are observed spanning a similar magnetic field range to compound **1**, indicating similar ZFS parameters; a subset of these spectra are plotted with respect to $B-B_c$ in Figure 7(b). In fact, the axial *D* parameter is about 15% larger than for **1**, as can be seen from the wider overall span of the spectra. Interestingly, it proved impossible to simultaneously reproduce the positions of the outer peaks/dips (relative to $B_c$) and the significant splitting observed within the central transitions using only second-order ZFS interactions: reproducing the splitting requires a significant reduction in $E/D$, but this creates a significant asymmetry in the outer peaks, i.e., one shifts toward $B_c$ and the other away. However, inclusion of a small fourth-order trigonal term ($B_4^3\hat{O}_4^3$, where $\hat{O}_4^3$ is an extended Stevens operator[77] and $B_4^3$ the associated coefficient, see Table 2) in the spin Hamiltonian reproduces the splitting without affecting the relative positions of the outer peaks/dips, leading to an excellent overall simulation. Likewise, simulations of the powder HFEPR spectra of **1** also improved upon inclusion of a small $B_4^3$ parameter (Table 2). Inclusion of such an interaction is not unreasonable given the intrinsic trigonal symmetry of the molecule. Indeed, similar interaction terms have been found for $d^5$ $Fe^{III}$ paramagnetic species doped into trigonal lattices.[78] Why such an interaction is needed for the powder simulations and not the solutions is unclear.

Overall, the HF-EPR studies of **1** and **6** paint a relatively consistent picture of the electronic structure of these TPR $Mn^{II}$ complexes. Perhaps the main surprise is the highly rhombic nature of the ZFS interaction parameters ($E/D \approx 0.33$), despite the molecules having such a high symmetry (trigonal) coordination geometry. However, it is important to recognize that the coordinating atoms are not equivalent, with two nitrogens and one oxygen making up the triangular faces of the trigonal prism. Therefore, in terms of metal−ligand interactions, the coordination geometry is far from being trigonal. Indeed, there is no apparent symmetry if one assumes significantly different metal−ligand interaction strengths for the coordinating oxygen and nitrogen atoms. For this reason, the rhombic electronic structure is not so surprising. ZFS parameters have been previously determined for a handful of the $Mn^{II}$ complexes which adopt a TPR geometry, Table S3.1. These complexes have values ranging from $D = 0.01-0.74$ $cm^{-1}$ and $E/D = 0-0.33$. For $Mn^{II}$, *D* is typically sensitive to the coordination number of the Mn center, with five-coordinate $Mn^{II}$ having large *D* parameters.[2,10] Duboc notes that for complexes containing halides the *D* parameter is controlled by the nature of the halide, $|D_{Cl}| < |D_{Br}| < |D_I|$, and for six-coordinate complexes with N,O-ligands the magnitude of the *D* parameter is dependent on the N/O ratio, $|D_{O_6}| < |D_{N_6}| \approx |D_{N_5O}|$. We find that this observation is true when considering those with TPR geometry, Table S3.1, and does not seem to depend on the ratio of N/O in the structures with mixed coordination spheres, $|D_{O_6}| < |D_{N_6}| \approx |D_{O_xN_{6-x}}|$. The $E/D$ ratio, which is typically a good probe of geometric distortion, was not found to be related to the nature of the ligands or the N/O ratio in previous studies.[2,10,79] In comparing the values in Table S3.1, we note that the $E/D$ ratio is not dependent on the N/O ratio nor on the value of CShM, but is however dependent on the asymmetry of the heteroplepticity of the ligand framework around the $Mn^{II}$ center. For example, complexes previously reported with the 1,1,1-tris[(3-methoxysalicylidene-amino)methyl]ethane ligand exhibit small values of $E/D \approx 0$. These ligands offer a more symmetric environment around the $Mn^{II}$ center, with a *pseudo*-3-fold rotational axis, despite the heteroleptic coordination sphere. In cases where there is a more asymmetric heterolepticity, such as **1** and **6**, the $E/D$ value approaches the rhombic limit of 0.333. In fact, this relationship of $E/D$ to heterolepticity can be expanded to $Mn^{II}$ complexes with a *mostly* octahedral geometry. Previously reported related $Mn^{II}$ compounds with similar hexadentate Schiff base ligands to those used in **1−9**, and thus similar asymmetric heterolepticity, $[Mn^{II}(5\text{-}NO_2\text{-}sal_2222)]$, $[Mn^{II}(5\text{-}NO_2\text{-}sal_2333)]$ and $[Mn^{II}(5\text{-}NO_2\text{-}sal_2323)]$,[80] have values of $D < 0.3$ $cm^{-1}$ with $E/D \approx 1/3$. As such it is likely that the origin of the high rhombicity in **1** and **6** originates from the asymmetric heteroleptic nature of the $Mn^{II}$ center coordination sphere.

## Comparison to Other Transition Metals

To determine the origin of the trigonal prismatic preference in **1−9** we compared these complexes to other transition metal complexes with the same general ligand (*R*-$sal_2$pipz) where structures with this ligand type for $Co^{II}$ ($d^7$ high-spin),[40,41] $Mn^{III}$ ($d^4$ high-spin),[42] $Fe^{III}$ ($d^5$ high-spin),[43] and $Co^{III}$ ($d^6$ low-spin)[42,44] are known. In addition to these we report a further

$Fe^{III}$ complex ($d^5$ high-spin), **10**, a $Ni^{II}$ complex ($d^8$ high-spin), **11**, and two $Zn^{II}$ ($d^{10}$) complexes, **12** and **13**. The structures of **10–13** are shown in Figure S2.3, and further crystallographic details are given in Tables S2.1 and S2.4. Plotting of all the known complexes of this ligand type with CShM(OC) versus CShM(TPR) (Figure S2.15, Table S2.11) reveals the highly flexible nature of this ligand, as it can support an almost ideal trigonal prism in the case of $Mn^{II}$ and $Fe^{III}$, and also support an almost ideal octahedron for $Co^{III}$, and all those geometries in between. The observed geometries follow the predicted $\Delta LFSE$ stabilization (Figure 1) for their respective $d^n$ configuration, with those transition metals with no electronic preference showing the lowest CShM(TPR) values. This suggests that the trigonal prismatic geometry is enforced by the ligand, except in the cases where there is a strong electronic preference for octahedral. However, the geometry can also vary depending on the substitution of the ligand. This is especially apparent in the $Zn^{II}$ complexes (**12** and **13**), where functionalization with a nitro group in the '3' position results in a CShM(TPR) value of 3.408, and that in the '5' position results in a value of 1.248. As such, the effect of ligand substitution and packing in crystalline samples needs to be considered as an additional barrier to geometric preferences.

## CONCLUSIONS

We have synthesized nine $Mn^{II}$ trigonal prismatic complexes using hexadentate Schiff base ligands of the *R*-sal$_2$pipz family. Continuous Shape Measures (CShM) were used to quantify the distortion around the $Mn^{II}$ centers, with CShM(TPR) values between 0.779 and 1.167, confirming the trigonal prismatic shape. We observed that those complexes with ligands functionalized with a nitro group in the '3' position stabilized a more ideal trigonal prismatic geometry. Trigonal prisms are typically rare for transition metals, even for $Mn^{II}$ which has no strong geometric preference. We have confirmed this through a search of the CSD, which revealed only 2.1% of published structures with $Mn^{II}$ contain a trigonal prismatic site (those with CShM(TPR) < 3). We have shown that the *R*-sal$_2$pipz ligand framework is highly flexible, it can adopt an octahedral or trigonal prismatic geometry which is largely dependent on the $\Delta LFSE$ stabilization (Figure 1) of the different $d^n$ configurations (Figure S2.15). In the case of $Mn^{II}$ the ligand enforces a trigonal prismatic geometry, with CShM(TPR) values ranging from 0.779 (**2a**) to 1.176 (**3a**). EPR measurements on **1** and **6** revealed ZFS parameters of $D = \pm 0.200\ \mathrm{cm}^{-1}$ ($E/D = 0.333$) for a solution sample of **1**, while $D = \pm 0.230\ \mathrm{cm}^{-1}$ ($E/D = 0.333$) for a powder sample of **6**. In both cases, the high degree of rhombicity, with $E/D$ values at the rhombic limit of 0.33, is likely due to the inequivalence of the coordinating atoms (oxygen and nitrogen) that make up the triangular faces of the trigonal prism. Electronic structure calculations will be needed to provide further insights. These complexes could offer a suitable reference for $Mn^{II}$ sites present in metalloenzymes with distorted geometries. The link between asymmetric heteroplepticity and the high degree of rhombicity could allow the description of the coordination sphere of unknown biological sites, and inform ligand design for $Mn^{II}$-based MRI contrast agents and complexes which exhibit slow magnetic relaxation.[81−88] These complexes could also offer suitable candidates for MCE behavior, taking advantage of the small ZFS, lack of magnetic interactions despite the relatively small intermolecular Mn−Mn distance, and the maximal spin, $S = 5/2$, for a 3d transition metal ion.

## ASSOCIATED CONTENT

### Supporting Information

The Supporting Information is available free of charge at https://pubs.acs.org/doi/10.1021/acs.inorgchem.5c05377.

> Synthetic methods, crystallographic details, additional crystal structure description, details of the Cambridge Structural Database (CSD) search, additional EPR spectra, UV−visible spectra, IR spectra, and additional magnetic characterization (PDF)

### Accession Codes

Deposition Numbers 2410990−2411004 contain the supplementary crystallographic data for this paper. These data can be obtained free of charge via the joint Cambridge Crystallographic Data Centre (CCDC) and Fachinformationszentrum Karlsruhe Access Structures service.

## AUTHOR INFORMATION

### Corresponding Authors

**Stephen Hill** − *Department of Physics and Department of Chemistry and Biochemistry, Florida State University, Tallahassee, Florida 32306, United States; National High Magnetic Field Laboratory, Florida State University, Tallahassee, Florida 32310, United States;* orcid.org/0000-0001-6742-3620; Email: shill@magnet.fsu.edu

**Grace G. Morgan** − *School of Chemistry, University College Dublin, Belfield, Dublin D04 N2E2, Ireland;* orcid.org/0000-0002-5467-0507; Email: grace.morgan@ucd.ie

### Authors

**Conor T. Kelly** − *School of Chemistry, University College Dublin, Belfield, Dublin D04 N2E2, Ireland;* orcid.org/0000-0003-0465-2412

**Brittany Grimm** − *Department of Physics, Florida State University, Tallahassee, Florida 32306, United States; National High Magnetic Field Laboratory, Florida State University, Tallahassee, Florida 32310, United States*

**Eimear Harrison** − *School of Chemistry, University College Dublin, Belfield, Dublin D04 N2E2, Ireland*

**Vibe B. Jakobsen** − *School of Chemistry, University College Dublin, Belfield, Dublin D04 N2E2, Ireland;* orcid.org/0000-0003-0671-092X

**Ross Jordan** − *School of Mathematics and Physics, Queen's University Belfast, Belfast BT7 1NN, U.K.*

**Solveig Felton** − *School of Mathematics and Physics, Queen's University Belfast, Belfast BT7 1NN, U.K.*

**Helge Müller-Bunz** − *School of Chemistry, University College Dublin, Belfield, Dublin D04 N2E2, Ireland*

Complete contact information is available at: https://pubs.acs.org/10.1021/acs.inorgchem.5c05377

### Author Contributions

The manuscript was written through contributions of all authors. All authors have given approval to the final version of the manuscript. Conceptualization: C.T.K., V.B.J., G.G.M.; Data Curation: C.T.K., E.H., B.G.; Formal Analysis: C.T.K., E.H., B.G., H.M.-B.; Funding Acquisition: S.F., S.H., G.G.M.; Investigation: C.T.K., E.H., B.G., V.B.J., R.J., H.M.-B.; Project Administration: S.H., G.G.M.; Resources: S.F., S.H., G.G.M.;

Supervision: S.F., S.H., G.G.M.; Visualization: C.T.K., B.G.; Writing—Original Draft: C.T.K., B.G.; Writing—Review and Editing: C.T.K., B.G., S.H., G.G.M.

### Notes

The authors declare no competing financial interest.

## ■ ACKNOWLEDGMENTS

This work was financially supported by the Irish Research Council (IRC) with Government of Ireland Postgraduate Scholarships (GOIPG/2016/73 to V.B.J. and GOIPG/2018/2510 to C.T.K.), Science Foundation Ireland (SFI) with a US-Ireland Award (19/US/3631 to G.G.M.) and a Frontiers for the Future Award (19/FFP/6909 to G.G.M.), University College Dublin for the UCD Advance PhD Supplemental Funding (to C.T.K. and G.G.M.), the Engineering and Physical Research Council (EP/L015323/1 to R.J.) through the PIADS CDT. Work performed in Florida was supported by the US National Science Foundation (NSF) through a counterpart US-Ireland-Northern Ireland R&D partnership (DMR-2004732 to S.H.), while work at the NHMFL is supported by the NSF (DMR-2128556) and the State of Florida. We thank Rónán Crowley, University College Dublin, for elemental analysis measurements.

## ■ REFERENCES

(1) Krzystek, J.; Ozarowski, A.; Telser, J. Multi-frequency, high-field EPR as a powerful tool to accurately determine zero-field splitting in high-spin transition metal coordination complexes. *Coord. Chem. Rev.* **2006**, *250* (17), 2308−2324.

(2) Duboc, C. Determination and prediction of the magnetic anisotropy of Mn ions. *Chem. Soc. Rev.* **2016**, *45* (21), 5834−5847.

(3) Zabala-Lekuona, A.; Seco, J. M.; Colacio, E. Single-Molecule Magnets: From Mn12-ac to dysprosium metallocenes, a travel in time. *Coord. Chem. Rev.* **2021**, *441*, No. 213984.

(4) Christou, G.; Gatteschi, D.; Hendrickson, D. N.; Sessoli, R. Single-Molecule Magnets. *MRS Bull.* **2000**, *25* (11), 66−71.

(5) Raza, A.; Perfetti, M. Electronic structure and magnetic anisotropy design of functional metal complexes. *Coord. Chem. Rev.* **2023**, *490*, No. 215213.

(6) Caravan, P.; Ellison, J. J.; McMurry, T. J.; Lauffer, R. B. Gadolinium(III) Chelates as MRI Contrast Agents: Structure, Dynamics, and Applications. *Chem. Rev.* **1999**, *99* (9), 2293−2352.

(7) Aime, S.; Botta, M.; Fasano, M.; Terreno, E. Lanthanide(III) chelates for NMR biomedical applications. *Chem. Soc. Rev.* **1998**, *27* (1), 19−29.

(8) Reis, M. S. Magnetocaloric and barocaloric effects of metal complexes for solid state cooling: Review, trends and perspectives. *Coord. Chem. Rev.* **2020**, *417*, No. 213357.

(9) Telser, J. Paramagnetic resonance investigation of mono- and di-manganese-containing systems in biochemistry. In *Methods in Enzymology*; Britt, R. D., Ed.; Academic Press, 2022; Vol. *666*, pp 315−372.

(10) Duboc, C.; Collomb, M.-N.; Neese, F. Understanding the zero-field splitting of mononuclear manganese(II) complexes from combined EPR spectroscopy and quantum chemistry. *Appl. Magn. Reson.* **2010**, *37* (1), 229−245.

(11) Pichon, C.; Mialane, P.; Rivière, E.; Blain, G.; Dolbecq, A.; Marrot, J.; Sécheresse, F.; Duboc, C. The Highest *D* Value for a $Mn^{II}$ Ion: Investigation of a Manganese(II) Polyoxometalate Complex by High-Field Electron Paramagnetic Resonance. *Inorg. Chem.* **2007**, *46* (19), 7710−7712.

(12) Un, S.; Dorlet, P.; Voyard, G.; Tabares, L. C.; Cortez, N. High-Field EPR Characterization of Manganese Reconstituted Superoxide Dismutase from Rhodobacter capsulatus. *J. Am. Chem. Soc.* **2001**, *123* (41), 10123−10124.

(13) Un, S.; Tabares, L. C.; Cortez, N.; Hiraoka, B. Y.; Yamakura, F. Manganese(II) Zero-Field Interaction in Cambialistic and Manganese Superoxide Dismutases and Its Relationship to the Structure of the Metal Binding Site. *J. Am. Chem. Soc.* **2004**, *126* (9), 2720−2726.

(14) Tabares, L. C.; Cortez, N.; Agalidis, I.; Un, S. Temperature-Dependent Coordination in *E. coli* Manganese Superoxide Dismutase. *J. Am. Chem. Soc.* **2005**, *127* (16), 6039−6047.

(15) Tabares, L. C.; Gätjens, J.; Un, S. Understanding the influence of the protein environment on the Mn(II) centers in Superoxide Dismutases using High-Field Electron Paramagnetic Resonance. *Biochim. Biophys. Acta, Proteins Proteomics* **2010**, *1804* (2), 308−317.

(16) Walsby, C. J.; Telser, J.; Rigsby, R. E.; Armstrong, R. N.; Hoffman, B. M. Enzyme Control of Small-Molecule Coordination in FosA as Revealed by $^{31}P$ Pulsed ENDOR and ESE-EPR. *J. Am. Chem. Soc.* **2005**, *127* (23), 8310−8319.

(17) Moomaw, E. W.; Angerhofer, A.; Moussatche, P.; Ozarowski, A.; García-Rubio, I.; Richards, N. G. J. Metal Dependence of Oxalate Decarboxylase Activity. *Biochemistry* **2009**, *48* (26), 6116−6125.

(18) Twahir, U. T.; Ozarowski, A.; Angerhofer, A. Redox Cycling, pH Dependence, and Ligand Effects of Mn(III) in Oxalate Decarboxylase from Bacillus subtilis. *Biochemistry* **2016**, *55* (47), 6505−6516.

(19) Campomanes, P.; Kellett, W. F.; Easthon, L. M.; Ozarowski, A.; Allen, K. N.; Angerhofer, A.; Rothlisberger, U.; Richards, N. G. J. Assigning the EPR Fine Structure Parameters of the Mn(II) Centers in Bacillus subtilis Oxalate Decarboxylase by Site-Directed Mutagenesis and DFT/MM Calculations. *J. Am. Chem. Soc.* **2014**, *136* (6), 2313−2323.

(20) Hadley, R. C.; Gagnon, D. M.; Ozarowski, A.; Britt, R. D.; Nolan, E. M. Murine Calprotectin Coordinates Mn(II) at a Hexahistidine Site with Ca(II)-Dependent Affinity. *Inorg. Chem.* **2019**, *58* (20), 13578−13590.

(21) Tóth, É.; Helm, L.; Merbach, A. E. Metal Complexes as MRI Contrast Enhancement Agents. In *Reference Module in Chemistry, Molecular Sciences and Chemical Engineering*; Elsevier, 2015.

(22) Platas-Iglesias, C.; Esteban-Gómez, D.; Helm, L.; Regueiro-Figueroa, M. Transient versus Static Electron Spin Relaxation in $Mn^{2+}$ Complexes Relevant as MRI Contrast Agents. *J. Phys. Chem. A* **2016**, *120* (32), 6467−6476.

(23) Li, Z.-Y.; Zhou, X.-Q.; Zhang, R.-R.; Zhang, X.-F.; Wu, D.-Q.; Zhai, B. A new approach to prepare the Mn(II)-based magnetic refrigerant through incorporating diamagnetic Cd(II) ion. *Inorg. Chim. Acta* **2020**, *506*, No. 119527.

(24) Wei, W.; Xie, R.-K.; Du, S.-W.; Tian, C.-B.; Chai, G.-L. Synthesis, structure, magnetocaloric effect and DFT calculations of a $Mn^{II}$ cluster-based inorganic coordination polymer. *J. Alloys Compd.* **2021**, *878*, No. 160353.

(25) Shang, Y.; Cao, Y.; Xie, Y.; Zhang, S.; Cheng, P. A 1D Mn-based coordination polymer with significant magnetocaloric effect. *Polyhedron* **2021**, *202*, No. 115173.

(26) Chen, Y.-C.; Guo, F.-S.; Liu, J.-L.; Leng, J.-D.; Vrábel, P.; Orendáč, M.; Prokleška, J.; Sechovský, V.; Tong, M.-L. Switching of the Magnetocaloric Effect of $Mn^{II}$ Glycolate by Water Molecules. *Chem.—Eur. J.* **2014**, *20* (11), 3029−3035.

(27) Cremades, E.; Echeverría, J.; Alvarez, S. The Trigonal Prism in Coordination Chemistry. *Chem.—Eur. J.* **2010**, *16* (34), 10380−10396.

(28) Smith, A. E.; Schrauzer, G. N.; Mayweg, V. P.; Heinrich, W. The Crystal and Molecular Structure of $MoS_6C_6H_6$. *J. Am. Chem. Soc.* **1965**, *87* (24), 5798−5799.

(29) Bailar, J. C. Some problems in the stereochemistry of coordination compounds: Introductory lecture. *J. Inorg. Nucl. Chem.* **1958**, *8* (C), 165−175.

(30) Aoki, S.; Sakurama, K.; Matsuo, N.; Yamada, Y.; Takasawa, R.; Tanuma, S.-i.; Shiro, M.; Takeda, K.; Kimura, E. A New Fluorescent Probe for Zinc(II): An 8-Hydroxy-5-*N,N*-dimethylaminosulfonylquinoline-Pendant 1,4,7,10-Tetraazacyclododecane. *Chem.—Eur. J.* **2006**, *12* (35), 9066−9080.

(31) Gyr, T.; Mäcke, H. R.; Hennig, M. A Highly Stable Silver(I) Complex of a Macrocycle Derived from Tetraazatetrathiacyclen. *Angew. Chem., Int. Ed.* **1997**, *36* (24), 2786−2788.

(32) Maumela, H.; Hancock, R. D.; Carlton, L.; Reibenspies, J. H.; Wainwright, K. P. The Amide Oxygen as a Donor Group. Metal Ion Complexing Properties of Tetra-*N*-acetamide Substituted Cyclen: A Crystallographic, NMR, Molecular Mechanics, and Thermodynamic Study. *J. Am. Chem. Soc.* **1995**, *117* (25), 6698−6707.

(33) Anderson, P. A.; Creaser, I. I.; Dean, C.; Harrowfield, J. M.; Horn, E.; Martin, L. L.; Sargeson, A. M.; Snow, M. R.; Tiekink, E. R. T. Synthesis, Resolution and Kinetics of Electron Self-Exchange of High-Spin Manganese(II)/(III) Cage Complexes. *Aust. J. Chem.* **1993**, *46* (4), 449−463.

(34) Khanra, S.; Weyhermüller, T.; Bill, E.; Chaudhuri, P. Deliberate Synthesis for Magnetostructural Study of Linear Tetranuclear Complexes $B^{III}Mn^{II}Mn^{II}B^{III}$, $Mn^{III}Mn^{II}Mn^{II}Mn^{III}$, $Mn^{IV}Mn^{II}Mn^{II}Mn^{IV}$, $Fe^{III}Mn^{II}Mn^{II}Fe^{III}$, and $Cr^{III}Mn^{II}Mn^{II}Cr^{III}$. Influence of Terminal Ions on the Exchange Coupling. *Inorg. Chem.* **2006**, *45* (15), 5911−5923.

(35) Parks, J. E.; Wagner, B. E.; Holm, R. H. Three-dimensional macrocyclic encapsulation reactions. I. Synthesis of six-coordinate complexes with nonoctahedral stereochemistry. *J. Am. Chem. Soc.* **1970**, *92* (11), 3500−3502.

(36) Parks, J. E.; Wagner, B. E.; Holm, R. H. Three-dimensional macrocyclic encapsulation reactions. II. Synthesis and properties of nonoctahedral clathro chelates derived from tris(2-aldoximo-6-pyridyl)phosphine and boron trifluoride or tetrafluoroborate. *Inorg. Chem.* **1971**, *10* (11), 2472−2478.

(37) Knight, J. C.; Alvarez, S.; Amoroso, A. J.; Edwards, P. G.; Singh, N. A novel bipyridine-based hexadentate tripodal framework with a strong preference for trigonal prismatic co-ordination geometries. *Dalton Trans.* **2010**, *39* (16), 3870−3883.

(38) Knight, J. C.; Amoroso, A. J.; Edwards, P. G.; Singh, N.; Ward, B. D. Shaping and enforcing coordination spheres: probing the ability of tripodal ligands to favour trigonal prismatic geometry. *Dalton Trans.* **2016**, *45* (26), 10630−10642.

(39) Wentworth, R. A. D.; Dahl, P. S.; Huffman, C. J.; Gillum, W. O.; Streib, W. E.; Huffman, J. C. Hindered-ligand systems. 9. Structure of the cis,cis-1,3,5-tris(pyridine-2-carboxaldimino)-cyclohexane complexes of cobalt(II) and zinc(II) ions. *Inorg. Chem.* **1982**, *21* (8), 3060−3063.

(40) Peng, Y.; Bodenstein, T.; Fink, K.; Mereacre, V.; Anson, C. E.; Powell, A. K. Magnetic anisotropy of a $Co^{II}$ single ion magnet with distorted trigonal prismatic coordination: Theory and experiment. *Phys. Chem. Chem. Phys.* **2016**, *18* (43), 30135−30143.

(41) Kubono, K.; Hirayama, N.; Kokusen, H.; Yokoi, K. Crystal Structure of {1,4-Bis[1-(3,5-dichlorophenolato-2-ylmethyl)-ylpropylamino-$\kappa^2$N,O]piperazine-$\kappa^2$N,N′}cobalt(II). *Anal. Sci.* **2003**, *19* (4), 645−646.

(42) Buta, I.; Ardelean, A.; Cseh, L.; Badea, V.; Manea, F.; Gal, E.; Lönnecke, P.; Hey-Hawkins, E.; Costisor, O. New mononuclear cobalt(III) and manganese(III) complexes containing a hexadentate Schiff base ligand. *Rev. Roum. Chim.* **2018**, *63* (5−6), 515−519.

(43) Butcher, R. J.; Pourian, M.; Jasinski, J. P. {1,4-Bis[3-(3-methoxy-2-oxidobenzylideneamino)propyl]piperazine}iron(III) tetrafluoridoborate. *Acta Crystallogr. Sect. E* **2007**, *63* (7), m1913−m1914.

(44) Cretu, C.; Cseh, L.; Tudose, R.; Bora, A.; Matsia, S.; Hatzidimitriou, A.; Costisor, O.; Salifoglou, A. Piperazine core-containing Schiff ligands define chemical reactivity toward divalent metal ions. *Inorg. Chim. Acta* **2019**, *492*, 249−261.

(45) Buta, I.; Shova, S.; Ilies, S.; Manea, F.; Andruh, M.; Costisor, O. Mono- and oligonuclear complexes based on a *o*-vanillin derived Schiff-base ligand: Synthesis, crystal structures, luminescent and electrochemical properties. *J. Mol. Struct.* **2022**, *1248*, No. 131439.

(46) Cretu, C.; Tudose, R.; Cseh, L.; Linert, W.; Halevas, E.; Hatzidimitriou, A.; Costisor, O.; Salifoglou, A. Schiff base coordination flexibility toward binary cobalt and ternary zinc complex assemblies. The case of the hexadentate ligand *N,N*′-bis[(2-hydroxybenzilideneamino)-propyl]-piperazine. *Polyhedron* **2015**, *85*, 48−59.

(47) Wentworth, R. A. D. Trigonal prismatic vs. octahedral stereochemistry in complexes derived from innocent ligands. *Coord. Chem. Rev.* **1972**, *9* (1), 171−187.

(48) CrysAlis$^{PRO}$ *Rigaku Oxford Diffraction*; Rigaku Corporation: Wroclaw, Poland, 2024.

(49) Clark, R. C.; Reid, J. S. The analytical calculation of absorption in multifaceted crystals. *Acta Crystallogr., Sect. A* **1995**, *51* (6), 887.

(50) Sheldrick, G. M. A short history of SHELX. *Acta Crystallogr., Sect. A* **2008**, *64*, 112−122.

(51) Sheldrick, G. M. SHELXT− Integrated space-group and crystal-structure determination. *Acta Crystallogr., Sect. A: Found. Adv.* **2015**, *71* (1), 3−8.

(52) Sheldrick, G. M. Crystal structure refinement with SHELXL. *Acta Crystallogr., Sect. C: Struct. Chem.* **2015**, *71* (1), 3−8.

(53) Groom, C. R.; Bruno, I. J.; Lightfoot, M. P.; Ward, S. C. The Cambridge Structural Database. *Acta Crystallogr., Sect. B: Struct. Sci. Cryst. Eng. Mater.* **2016**, *72* (2), 171−179.

(54) Bruno, I. J.; Cole, J. C.; Edgington, P. R.; Kessler, M.; Macrae, C. F.; McCabe, P.; Pearson, J.; Taylor, R. New software for searching the Cambridge Structural Database and visualizing crystal structures. *Acta Crystallogr., Sect. B: Struct. Sci.* **2002**, *58* (3), 389−397.

(55) Brown, I. D. *The Chemical Bond in Inorganic Chemistry: The Bond Valence Model*; Oxford University Press, 2002.

(56) Brown, I. D. *Bond Valence Parameters*, https://www.iucr.org/resources/data/datasets/bond-valence-parameters. (accessed 01/01/2026).

(57) *SHAPE: Program for the Stereochemical Analysis of Molecular Fragments by Means of Continuous Shape Measures and Associated Tools*; Universitat de Barcelona: Barcelona, Spain, 2013.

(58) Hassan, A. K.; Pardi, L. A.; Krzystek, J.; Sienkiewicz, A.; Goy, P.; Rohrer, M.; Brunel, L. C. Ultrawide Band Multifrequency High-Field EMR Technique: A Methodology for Increasing Spectroscopic Information. *J. Magn. Reson.* **2000**, *142* (2), 300−312.

(59) Alvarez, S.; Alemany, P.; Casanova, D.; Cirera, J.; Llunell, M.; Avnir, D. Shape maps and polyhedral interconversion paths in transition metal chemistry. *Coord. Chem. Rev.* **2005**, *249* (17), 1693−1708.

(60) Alvarez, S.; Avnir, D.; Llunell, M.; Pinsky, M. Continuous symmetry maps and shape classification. The case of six-coordinated metal compounds. *New J. Chem.* **2002**, *26* (8), 996−1009.

(61) Zabrodsky, H.; Peleg, S.; Avnir, D. Continuous symmetry measures. *J. Am. Chem. Soc.* **1992**, *114* (20), 7843−7851.

(62) Casanova, D.; Cirera, J.; Llunell, M.; Alemany, P.; Avnir, D.; Alvarez, S. Minimal Distortion Pathways in Polyhedral Rearrangements. *J. Am. Chem. Soc.* **2004**, *126* (6), 1755−1763.

(63) Cirera, J.; Ruiz, E.; Alvarez, S. Shape and Spin State in Four-Coordinate Transition-Metal Complexes: The Case of the d$^6$ Configuration. *Chem.—Eur. J.* **2006**, *12* (11), 3162−3167.

(64) Arulsamy, N.; Glerup, J.; Hodgson, D. J. Mononuclear Iron(II), Manganese(II), and Nickel(II) and Tetranuclear Iron(III) Complexes of a New Hexadentate Ligand. *Inorg. Chem.* **1994**, *33* (14), 3043−3050.

(65) Biswas, S.; Mitra, K.; Chattopadhyay, S. K.; Adhikary, B.; Lucas, C. R. Mononuclear manganese(II) and manganese(III) complexes of $N_2O$ donors involving amine and phenolate ligands: absorption spectra, electrochemistry and crystal structure of $[Mn(L_3)_2](ClO_4)$. *Transition Met. Chem.* **2005**, *30* (4), 393−398.

(66) Kuppayee, M.; Kumaran, D.; Ponnuswamy, M. N.; Kandaswamy, M.; Violet, M. J.; Chinnakali, K.; Fun, H. K. 1,4-Bis(2-hydroxy-5-methylbenzyl)piperazine. *Acta Crystallogr., Sect. C: Cryst. Struct. Commun.* **1999**, *55* (12), 2147−2149.

(67) Cremer, D.; Pople, J. A. General definition of ring puckering coordinates. *J. Am. Chem. Soc.* **1975**, *97* (6), 1354−1358.

(68) Cremer, D. On the correct usage of the Cremer-Pople puckering parameters as quantitative descriptors of ring shapes - a reply to recent criticism by Petit, Dillen and Geise. *Acta Crystallogr., Sect. B: Struct. Sci.* **1984**, *40* (5), 498−500.

(69) Spackman, M. A.; Jayatilaka, D. Hirshfeld surface analysis. *CrystEngComm* **2009**, *11* (1), 19−32.

(70) Spackman, M. A.; McKinnon, J. J. Fingerprinting intermolecular interactions in molecular crystals. *CrystEngComm* **2002**, *4* (66), 378−392.

(71) Spackman, P. R.; Turner, M. J.; McKinnon, J. J.; Wolff, S. K.; Grimwood, D. J.; Jayatilaka, D.; Spackman, M. A. CrystalExplorer: a program for Hirshfeld surface analysis, visualization and quantitative analysis of molecular crystals. *J. Appl. Crystallogr.* **2021**, *54* (3), 1006−1011.

(72) Stoll, S.; Schweiger, A. EasySpin, a comprehensive software package for spectral simulation and analysis in EPR. *J. Magn. Reson.* **2006**, *178* (1), 42−55.

(73) Boča, R. Zero-field splitting in metal complexes. *Coord. Chem. Rev.* **2004**, *248*, 757−815.

(74) Bou-Abdallah, F.; Chasteen, N. D. Spin concentration measurements of high-spin (g′ = 4.3) rhombic iron(III) ions in biological samples: theory and application. *J. Biol. Inorg. Chem.* **2007**, *13* (1), 15−24.

(75) van Gorkum, R.; Buda, F.; Kooijman, H.; Spek, A. L.; Bouwman, E.; Reedijk, J. Trigonal-Prismatic vs. Octahedral Geometry for $Mn^{II}$ Complexes with Innocent Didentate Ligands: A Subtle Difference as Shown by XRD and DFT on $[Mn(acac)_2(bpy)]$. *Eur. J. Inorg. Chem.* **2005**, *2005*, 2255−2261.

(76) Birdy, R. B.; Goodgame, M. Electron spin resonance study of manganese(II) ions in trigonal-prismatic coordination in tris-(acetylacetonato)metal(II) anions. *Inorg. Chem.* **1979**, *18* (2), 472−475.

(77) Marbey, J.; Gan, P.-R.; Yang, E.-C.; Hill, S. Magic-angle effects in a trigonal $Mn_3^{III}$ cluster: Deconstruction of a single-molecule magnet. *Phys. Rev. B* **2018**, *98* (14), No. 144433.

(78) Vazhenin, V. A.; Guseva, V. B.; Artyomov, M. Y.; Route, R. K.; Fejer, M. M.; Byer, R. L. Fine structure of the electron paramagnetic resonance spectrum of $Fe^{3+}$ centres in $LiTaO_3$. *J. Phys.: Condens. Matter* **2003**, *15* (2), 275.

(79) Rich, J.; Castillo, C. E.; Romero, I.; Rodríguez, M.; Duboc, C.; Collomb, M.-N. Investigation of the Zero-Field Splitting in Six- and Seven-Coordinate Mononuclear $Mn^{II}$ Complexes with N/O-Based Ligands by Combining EPR Spectroscopy and Quantum Chemistry. *Eur. J. Inorg. Chem.* **2010**, *2010* (23), 3658−3665.

(80) Mabad, B.; Cassoux, P.; Tuchagues, J. P.; Hendrickson, D. N. Manganese(II) complexes of polydentate Schiff bases. 1. Synthesis, characterization, magnetic properties, and molecular structure. *Inorg. Chem.* **1986**, *25* (9), 1420−1431.

(81) Wang, L.-X.; Wu, X.-F.; Jin, X.-X.; Li, J.-Y.; Wang, B.-W.; Liu, J.-Y.; Xiang, J.; Gao, S. Slow magnetic relaxation in 8-coordinate Mn(II) compounds. *Dalton Trans.* **2023**, *52* (41), 14797−14806.

(82) Pilichos, E.; Font-Bardia, M.; Aullón, G.; Mayans, J.; Escuer, A. Family of Quasi-Isotropic $Mn^{II}$ and $Mn_2^{II}$ Complexes Exhibiting Slow Relaxation of the Magnetization. *Inorg. Chem.* **2024**, *63* (43), 20415−20426.

(83) Rajnák, C.; Titiš, J.; Moncol, J.; Mičová, R.; Boča, R. Field-Induced Slow Magnetic Relaxation in a Mononuclear Manganese(II) Complex. *Inorg. Chem.* **2019**, *58* (2), 991−994.

(84) Hay, M. A.; Sarkar, A.; Marriott, K. E. R.; Wilson, C.; Rajaraman, G.; Murrie, M. Investigation of the magnetic anisotropy in a series of trigonal bipyramidal Mn(II) complexes. *Dalton Trans.* **2019**, *48* (41), 15480−15486.

(85) da Cunha, T. T.; Barbosa, V. M. M.; Oliveira, W. X. C.; Pedroso, E. F.; García, D. M. A.; Nunes, W. C.; Pereira, C. L. M. Field-Induced Slow Magnetic Relaxation of a Six-Coordinate Mononuclear Manganese(II) and Cobalt(II) Oxamate Complexes. *Inorg. Chem.* **2020**, *59* (18), 12983−12987.

(86) Legendre, C. M.; Lüert, D.; Herbst-Irmer, R.; Stalke, D. Benchmarking magnetic and spectroscopic properties on highly stable 3d metal complexes with tuneable bis(benzoxazol-2-yl)methanide ligands. *Dalton Trans.* **2021**, *50* (45), 16810−16818.

(87) Rok, M.; Zarychta, B.; Janicki, R.; Witwicki, M.; Bieńko, A.; Bator, G. Dielectric-Optical Switches: Photoluminescent, EPR, and Magnetic Studies on Organic−Inorganic Hybrid $(azetidinium)_2MnBr_4$. *Inorg. Chem.* **2022**, *61* (14), 5626−5636.

(88) Mičová, R.; Rajnák, C.; Titiš, J.; Samoľová, E.; Zalibera, M.; Bieńko, A.; Boča, R. Slow magnetic relaxation in two mononuclear Mn(II) complexes not governed by the over-barrier Orbach process. *Chem. Commun.* **2023**, *59* (18), 2612−2615.